magnetochemistry

MDPI

Supplementary Materials

Mononuclear Lanthanide(III)-Salicylideneaniline Complexes: Synthetic, Structural, Spectroscopic, and Magnetic Studies †

Further Points of Synthetic Interest

Points of synthetic interest are: (i) The experimental reaction ratio used for the preparation of the twenty two complexes is not the same with the stoichiometric ratio found in the products [Ln^{III}: salanH = 1:2 for **1**·MeCN_Pr–**11**·MeCN_Y and 1:3 for **12**_Pr–**22**_Y]; the stoichiometric reaction ratios, however, lead to the same products in comparable yields, as proven by IR spectra. (ii) Addition of external bases in the reaction systems changes the chemistry completely; the obtained powders in MeCN and MeOH have IR spectra different from those of **1**·MeCN_Pr–**11**·MeCN_Y and **12**_Pr–**22**_Y, respectively. (iii) The 1:1 and 1:2 reactions of $Ln(NO_3)_3{\cdot}xH_2O$ (Ln = La, Ce) and salanH in MeCN and MeOH give powders with IR spectra and pXRD patterns that do not match with those of **1**·MeCN_Pr–**11**·MeCN_Yand **12**_Pr–**22**_Y, suggesting a chemical and structural change; also the crystallization behavior of the La(III) and Ce(III) materials is not analogous with that of the other complexes and therefore we could not isolate single crystals for full X-ray diffraction analysis;and (iv) The reaction mixtures in MeOH that lead to complexes **12**_Pr–22_Y change color upon storage in closed vials as a function of time. In the first 2–3 days the color is yellowish orange and the obtained crystals correspond to products **12**_Pr–**22**_Y. After ~ 3 days the color of the supernatant solution begins to darken and after 1 week it is dark brown. Meanwhile a single crystal-to-single crystal transformation takes place. A full data set was collected on the new orange (albeit darker than that of **18**_Dy) single crystal from the $Dy(NO_3)_3{\cdot}5H_2O$/salanH reaction mixture. The preliminary solution of the structure revealed the formula $[Dy(NO_3)_3(salanH)_2(MeOH)]$, suggesting the decomposition represented by Equation (1). The full characterization of this new product is in progress and our initial results indicate that this compound is the first member of a third family of mononuclear complexes from the $Ln(NO_3)_3{\cdot}xH_2O$/salanH reaction system.

$$\left[Dy(NO_3)_3(salanH)_2(MeOH)\right](salanH) \xrightarrow[1week]{MeOh} \left[Dy(NO_3)_3(salanH)_2(MeOH)\right] + salanH \qquad (1)$$

Full Spectroscopic (IR, ^{1}H NMR for the Y^{iii} Complexes, Diffuse Reflectance for Selected Compounds) Studies

The IR spectra of the complexes (Figures S2 and S3) exhibit a medium-intensity broad band at ~3400 cm^{-1} (the spectra of **1**_Pr-**11**_Y also exhibit a submaximu at ~ 3250 cm^{-1}), attributed to the ν(OH) vibration of the coordinated solvent molecule (H_2O in **1**_Pr-**11**_Yand MeOH in **12**_Pr–**22**_Y) and to the $\nu(NH^+)$ vibration of the zwitterionic salanH ligand and the lattice salanH molecule (in **12**_Pr–**22**_Y) (*vide infa*). The spectra of the complexes exhibit a strong band at 1636 (**1**_Pr-**11**_Y) and 1638 (**12**_Pr–**22**_Y) cm^{-1}. At first glance, this band can be assigned to the ν(C=N) vibration of the imine (i.e., Schiff base) linkage [1,2]. This band has been shifted to higher wavenumbers on going from the free salanH (at 1616 cm^{-1} [2]) to the complexes. Such a behavior is not typical of the protonation of an imine nitrogen (the nitrogen atom is protonated and hence uncoordinated in the complexes, *vide infra*). Combined with the facts that the aromatic carbon-oxygen and aliphatic carbon-nitrogen bond lengths in the complexes are shorter and longer, respectively, compared with the corresponding bond distances in the free ligand [3–6], this spectral behavior makes us strongly believe that the band at 1636–1638 cm^{-1} has a partial double carbon-oxygen stretching vibration character [$\upsilon(\overset{-}{C}\cdots O)$] and the coordinated salanH ligand thus exhibits a partial *cis*-keto (or *cis*-keto-amine) character in **1**_Pr–**22**_Y [7]. We would like to emphasize that this conclusion is tentative because the IR spectra of both

the complexes and free salanH have been recorded at room temperature, whereas most of the structures of salanH have been solved at lower temperatures. An alternative assignment of the 1636–1638 cm^{-1} band [2] would be as ν(C=NH^+), since the strong intra molecular O-H⋯N hydrogen bond in the structures of the free salanH compound decreases the aliphatic carbon-nitrogen force constant and thus the ν(C=N) vibration is at a rather low wavenumber (at 1616 cm^{-1}). In the KBr IR spectra of **1**_Pr-**11**_Y, the bands at 1482, 1288 and 1010 cm^{-1} are assigned [8] to the $\nu_1(A_1)[\nu(N{=}O)]$, $\nu_5(B_2)[\nu_{as}(NO_2)]$ and $\nu_2(A_1)[\nu_s(NO_2)]$ vibrational modes, respectively, of the coordinated nitrato groups. The separation of the two highest-wavenumber stretching bands is ~200 cm^{-1}, indicating the presence of bidentate nitrato ligands of C_{2v} symmetry [8]. The corresponding bands in the spectra of **12**_Pr–**22**_Y are located at ~1490, ~1285 and ~1020 cm^{-1}. The KBr spectra of all the complexes exhibit a medium-to-strong intensity band at 1384 cm^{-1}, assigned to the $\nu_3(E')[\nu_d(NO)]$ vibrational fundamental of the planar ionic nitrate of D_{3h} symmetry [8]. The appearance of this band suggests that a certain amount of nitrato groups is replaced by bromides that are in excess in the KBr matrix, therefore producing ionic nitrates (KNO_3); this replacement is facilitated by the applied pressure during the preparation of the KBr pellets. As expected, the band at 1384 cm^{-1} does not appear in the mull spectra of **1**_Pr–**22**_Y.

The diamagnetic nature of the Y(III) complexes **11**_Yand **22**_Ygave us the opportunity to study their solution behavior. The ^{1}H NMR spectra of complexes **11_Y** and **22_Y**in DMSO-d_6 (Figure S4 and Figure S5) are almost identical with the spectrum of free salanH in the same solvent (Figure S6). The only differences are: (a) The slightly sharper character of the ligands' –OH signal at δ 13.08 ppm in **11**_Yand **22**_Ycompared with that of free salanH. (b) The appearance of an extra signal at δ 3.30 ppm (very close to the main H_2O signal from the deuteriated solvent at δ 3.32 ppm) in the spectrum of **11**_Y, attributed to the H_2O molecule that is present in the compound. (c) The appearance of an extra signal at δ 2.08 ppm in the spectrum of **11**_Y, due to the methyl hydrogen atoms of the residual lattice MeCN that remained in the sample after drying; and (d) The appearance of an extra doublet at δ 3.17 ppm and an extra multiplet at δ 4.09 ppm in the spectrum of **22**_Y, attributed to the methyl and hydroxyl protons, respectively, of the MeOH molecule that is present in the complex. The spectra show the signal of the proton attached to the imino carbon atom at δ8.96 ppm and the aromatic protons in the δ 7.67–6.96 ppm region with the expected integration ratio [9]. The data indicate that **11**_Y and **22**_Y decompose in solution releasing the salanH ligands (and possibly the nitrato groups), the coordination sphere of Y^{III} being satisfied or completed by DMSO molecules [7]. The spectra could not be recorded in $CDCl_3$ (a non-coordinating solvent) because of solubility problems.

The solid-state (diffuse reflectance) spectra of selected complexes have been recorded in the 400–1600 nm range (Figure S6). The spectra are dominated by a broad intraligand band at ~500 nm; this transition has been shifted to longer wavelengths by ~100 nm compared with the absorption of the free salanH (at 390 nm), due to coordination [10]. In the spectra of a few complexes, some f-f transitions could be seen as weak, rather sharp bands and these have been assigned on the basis of the well characterized energy-level diagrams for the Ln^{III} ions concerned. Specific assignments [7,11] for representative complexes are listed below. Pr(III) complexes: $^3D_4\rightarrow{}^1D_2$ (592 nm for both **1**_Pr and **12**_Pr; the $^3H_4\rightarrow{}^3P_0$ and $^3H_4\rightarrow{}^3P_2$ transitions are masked by the intraligand absorption; $^3H_4\rightarrow{}^3F_4$ (1450 nm for **1**_Pr and 1455 nm for **12**_Pr);$^3H_4\rightarrow{}^3F_3$ (1570 nm for both **1**_Pr and **12**_Pr). Nd(III) complexes: $^4I_{9/2}\rightarrow{}^4G_{5/2}$,$^2G_{7/2}$ (582/589/602 nm for **2**_Nd and 579/583/601 nm for **13**_Nd); $^4I_{9/2}\rightarrow{}^4F_{9/2}$ (691 nm for **2**_Nd and 693 nm for **13**_Nd); $^4I_{9/2}\rightarrow{}^4F_{7/2}$, $^4S_{3/2}$ (744/761 nm for **2**_Nd and 755/760/777 nm for **13**_Nd); $^4I_{9/2}\rightarrow{}^4F_{5/2}$, $^2H_{9/2}$ (800/812 nm for **2**_Nd and 802/815 nm for **13**_Nd); $^4I_{9/2}\rightarrow{}^4F_{3/2}$ (876 nm for **2**_Ndand 881 nm for **13**_Nd). Sm(III) complexes: $^6H_{5/2}\rightarrow{}^6F_{11/2}$ (950 nm for both **3**_Sm and **14**_Sm); $^6H_{5/2}\rightarrow{}^4F_{9/2}$ (1080 nm for **3**_Sm and 1082 nm for **14**_Sm); $^6H_{5/2}\rightarrow{}^4F_{7/2}$ (1240 nm for **3**_Sm and 1235 nm for **14**_Sm); $^6H_{5/2}\rightarrow{}^4F_{5/2}$ (1395 nm for both **3**_Sm and **14**_Sm); $^6H_{5/2}\rightarrow{}^4F_{3/2}$ (1505 nm for **3**_Sm and 1502 nm for **14**_Sm); $^6H_{15/2}\rightarrow{}^4F_{1/2}$ (1560 nm for **3**_Sm and 1555 nm for **14**_Sm). Er(III) complexes: $^4I_{15/2}\rightarrow{}^4F_{9/2}$ (658 nm for **9**_Erand 654 nm for **20**_Er);$^4I_{15/2}\rightarrow{}^4I_{11/2}$ (980 nm for both **9**_Er and **20**_Er); $^4I_{15/2}\rightarrow{}^4I_{13/2}$ (1495 nm for **9**_Er and 1505 nm for **20**_Er).

Table S1. Continuous Shape Measures (CShM) values for the potential coordination polyhedra of the Ln^{III} center in the structures of complexes **4**·MeCN_Eu, **7**·MeCN_Dy and **10**·MeCN_Yb.[a]

Ideal Coordination Polyhedron	4·MeCN_Eu	7·MeCN_Dy	10·MeCN_Yb
Enneagon (EP-9)	34.481	34.501	34.485
Octagonal pyramid (OPY-9)	23.803	23.613	23.487
Heptagonal bipyramid (HBPY-9)	18.562	18.711	18.818
Johnson triangular cupola (JTC-9)	13.207	13.226	13.173
Capped cube (JCCU-9)	9.449	9.457	9.483
Spherical-relaxed capped cube (CCU-9)	8.314	8.373	8.464
Capped square antiprism (JCSAPR-9)	3.651	3.495	3.377
Spherical capped square antiprism (CSAPR-9)	2.587	2.437	2.358
Tricapped trigonal prism (JTCPR-9)	3.177	2.922	2.730
Spherical tricapped trigonal prism (TCTPR-9)	**2.249**	**2.108**	**1.996**

[a] The polyhedron with the smallest CShM value (in bold) is the real coordination polyhedron of the Ln^{III} center for the complex.

Table S2. Continuous Shape Measures (CShM) values for the potential coordination polyhedra of the Ln^{III} center in the structures of complexes **17**_Tb and **18**_Dy.[a]

Ideal Coordination Polyhedron	17_Tb	18_Dy
Enneagon (EP-9)	33.812	33.817
Octagonal pyramid (OPY-9)	22.850	22.803
Heptagonal bipyramid (HBPY-9)	18.018	18.064
Johnson triangular cupola (JTC-9)	14.614	14.553
Capped cube (JCCU-9)	10.748	10.726
Spherical-relaxed capped cube (CCU-9)	9.478	9.465
Capped square antiprism (JCSAPR-9)	2.618	2.569
Spherical capped square antiprism (CSAPR-9)	**1.860**	**1.819**
Tricapped trigonal prism (JTCPR-9)	3.757	3.670
Spherical tricapped trigonal prism (TCTPR-9)	2.951	2.879

[a] The polyhedron with the smallest CShM value (in bold) is the real coordination polyhedron of the LnIII center for the complex.

Table S3. H-bonding interactions in the crystal structures of complexes **4**·MeCN_Eu, **7**·MeCN_Dy and **10**·MeCN_Yb.

D-H···A	D-H (Å)	H···A (Å)	D···A (Å)	D-H···A (°)
		Compound **4**·MeCN_Eu		
N1-H(N1)···O1	0.76(2)	1.98(2)	2.619(2)	141(2)
N2-H(N2)···O2	0.82(2)	2.01(2)	2.666(2)	137(2)
O1W-H_B(O1W)···N6	0.73(3)	2.13(3)	2.848(3)	169(3)
O1W-H_A(O1W)···O6′[a]	0.78(3)	2.07(3)	2.855(2)	177(3)
C28-H_B(C28)···O4′′[b]	0.98	2.48	3.258(3)	135.9
C13-H(C13)···O8′′′[c]	0.93(3)	2.58(3)	3.493(2)	166(2)
		Compound **7**·MeCN_Dy		
N1-H(N1)···O1	0.91(4)	1.84(5)	2.609(4)	140(4)
N2-H(N2)···O2	0.70(4)	2.10(4)	2.676(5)	140(5)
O1W-H_B(O1W)···N6	0.71(6)	2.16(6)	2.863(7)	169(7)
O1W-H_A(O1W)···O6′[a]	0.81(5)	2.05(5)	2.850(4)	169(5)
C28-H_B(C28)···O4′′[b]	0.98	2.53	3.272(6)	132
C13-H(C13)···O8′′′[c]	0.78(4)	2.77(5)	3.516(6)	160(4)

Compound **10**·MeCN_Yb				
N1-H(N1)···O1	0.77(2)	1.98(2)	2.614(2)	139(2)
N2-H(N2)···O2	0.75(3)	2.09(3)	2.677(2)	136(3)
O1W-H_B(O1W)···N6	0.79(3)	2.09(3)	2.856(3)	163(3)
O1W-H_A(O1W)···O6′[a]	0.72(3)	2.15(3)	2.868(2)	176(3)
C28-H_B(C28)···O4′′[b]	0.98	2.50	3.282(3)	136.6
C13-H(C13)···O8′′′[c]	0.94(2)	2.58(2)	3.505(2)	167(2)

[a] Symmetry code of O6′: $-x+2, -y, -z+1$; [b] Symmetry code of O4′′: $x, y-1, z$; [c] Symmetry code of O8′′′: $x-1, y, z$. Atom C28 is the methyl carbon atom of the lattice MeCN molecule. D = donor; A = acceptor.

Table S4. H-bonding interactions in the crystal structures of complexes **17**_Tb and **18**_Dy.

D-H···A	D-H (Å)	H···A (Å)	D···A (Å)	D-H···A (°)
Compound **17**_Tb				
N1-H(N1)···O1	0.96(8)	1.94(8)	2.663(6)	131(6)
N1-H(N1)···O6	0.96(8)	2.44(8)	3.160(6)	132(6)
N2-H(N2)···O2	0.84(6)	1.95(6)	2.647(6)	140(6)
N6-H(N6)···O13	0.88	1.76	2.503(6)	141
C2-H(C2)···O12	0.90(6)	2.56(6)	3.361(7)	149(5)
C15-H(C15)···O12	0.92(6)	2.48(6)	3.325(6)	151(5)
O12-H(O12)···O13[a]	0.83(7)	1.74(7)	2.558(6)	167(7)
C36-H(C36)···O11	0.85(5)	2.69(5)	3.481(8)	156(4)
Compound **18**_Dy				
N1-H(N1)···O1	0.89(5)	1.96(5)	2.667(4)	135(4)
N1-H(N1)···O6	0.89(5)	2.50(5)	3.156(4)	131(4)
N2-H(N2)···O2	0.90(5)	1.90(5)	2.640(4)	139(5)
N6-H(N6)···O13	0.88	1.76	2.504(4)	141
C2-H(C2)···O12	0.92(4)	2.57(4)	3.353(4)	144(3)
C15-H(C15)···O12	0.94(4)	2.49(4)	3.309(4)	146(4)
O12-H(O12)···O13[a]	0.66(5)	1.91(5)	2.549(4)	162(6)
C36-H(C36)···O11	0.99(4)	2.53(5)	3.472(6)	160(3)

[a] Symmetry code: $-x, -y+2, -z+2$. Atoms C2 and C15 (not labelled in the various figures) are aromatic carbon atoms that belong to the benzylidene (phenolate) rings of the two coordinated salanH ligands, while atom C36 is an aromatic carbon atom that belongs to the aniline ring of the lattice salanH molecule.

Table S5. Crystallographic data for complexes 4·MeCN_Eu, 7·MeCN_Dy, 10·MeCN_Yb, 17_Tb and 18_Dy.

Parameter	4·MeCN_Eu	7·MeCN_Dy	10·MeCN_Yb	17_Tb	18_Dy
Formula	$C_{28}H_{27}N_6EuO_{12}$	$C_{28}H_{27}N_6DyO_{12}$	$C_{28}H_{27}N_6O_{12}Yb$	$C_{40}H_{37}N_6TbO_{13}$	$C_{40}H_{37}N_6DyO_{13}$
Formula weight	791.51	802.05	812.59	968.67	972.25
Crystal system	triclinic	triclinic	triclinic	triclinic	triclinic
Space group	*P*-1	*P*-1	*P*-1	*P*-1	*P*-1
Radiation	Mo Kα	Cu Kα	Mo Kα	Cu Kα	Cu Kα
T/K	170	160	160	160	160
a/Å	10.6060(2)	10.5411(2)	10.4906(2)	9.5979(2)	9.5959(2)
b/Å	11.7294(2)	11.6960(2)	11.6573(2)	10.1218(2)	10.1104(2)
c/Å	14.0769(3)	14.0507(3)	14.0419(3)	22.6686(4)	22.6646(4)

α/°	77.147(1)	77.044(1)	76.943(1)	78.237(1)	78.225(1)
β/°	73.649(1)	73.591(1)	73.509(1)	87.035(1)	87.018(1)
γ/°	71.219(1)	71.330(1)	71.454(1)	62.990(1)	62.947(1)
V/Å^3	1574.06(5)	1557.14(5)	1543.59(5)	1918.70(7)	1914.99(7)
Z	2	2	2	2	2
D_{calcd}/g cm^{-3}	1.670	1.711	1.748	1.677	1.686
μ/mm^{-1}	2.06	13.48	3.10	9.73	11.10
$2\vartheta_{max}$/°	54.0	130.0	55.0	130.0	130.0
Reflections collected	29769	35159	30735	30553	34271
Reflections unique (R_{int})	6865(0.025)	5028(0.089)	7079(0.026)	6196(0.060)	6195(0.063)
Reflections with $I > 2\sigma(I)$	6553	4725	6711	5434	5736
No. of parameters	518	519	518	670	670
R_1[a][$I > 2\sigma(I)$]	0.0185	0.0401	0.0166	0.0484	0.0355
wR_2[b](all data)	0.0454	0.0821	0.0398	0.1224	0.0773
GOF(F^2)	1.08	1.04	1.05	1.12	1.06
$\Delta\rho_{max}/\Delta\rho_{min}$ (e Å^{-3})	0.68/−0.48	1.42/−1.89	0.60/−0.32	1.39/−1.18	1.29/−1.42
CCDC	1863571	1863570	1863572	1863568	1863569

[a]$R_1 = \Sigma(|F_o| - |F_c|)/\Sigma(|F_o|)$; [b]$wR_2 = \{\Sigma[w(F_o^2 - F_c^2)]/\Sigma[w(F_o^2)^2]\}^{1/2}$.

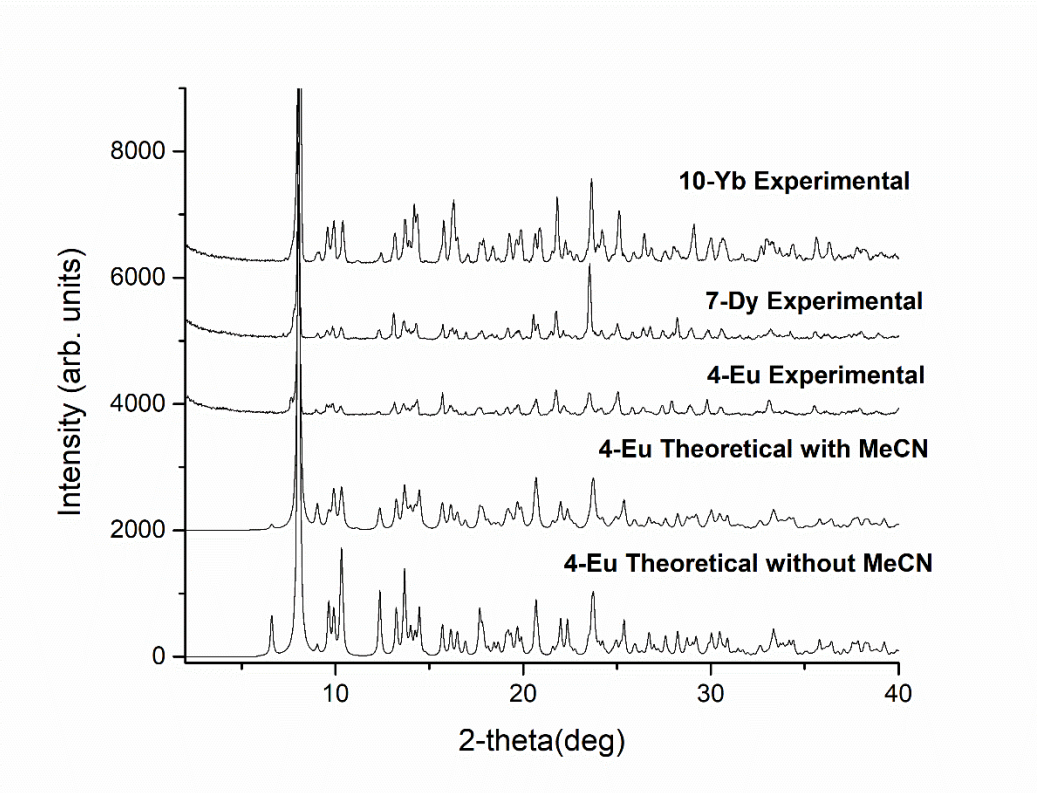

Figure S1. Experimental X-ray diffraction patterns of freshly prepared and well dried powders of complexes **4**·MeCN_Eu (labelled as **4-Eu Experimental**), **7**·MeCN_Dy (labelled as **7-Dy Experimental**) and **10**·MeCN_Yb (labelled as **10-Yb Experimental**). The simulated pattern of the structurally characterized Eu(III) complex **4**·MeCN_Eu(labelled as **4-Eu Theoretical with MeCN**) and the calculated pattern of the same complex after removing the solvent atoms from the .cif (labelled as **4-Eu Theoretical without MeCN**).

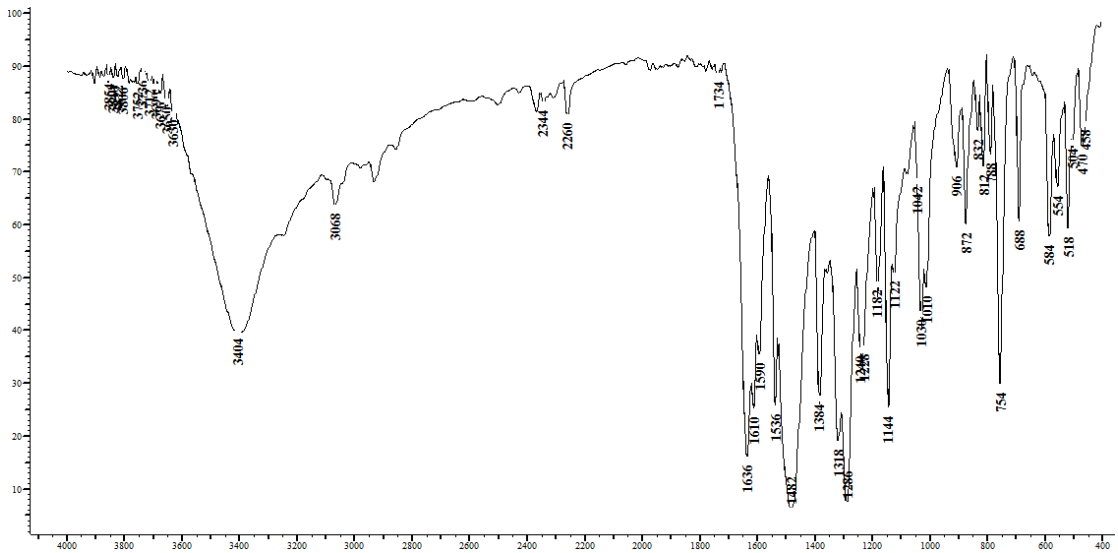

Figure S2. The IR spectrum (KBr, cm^{-1}) of a well dried sample of complex $[Dy(NO_3)_3(salanH)_2(H_2O)]$·MeCN (**7**·MeCN_Dy).

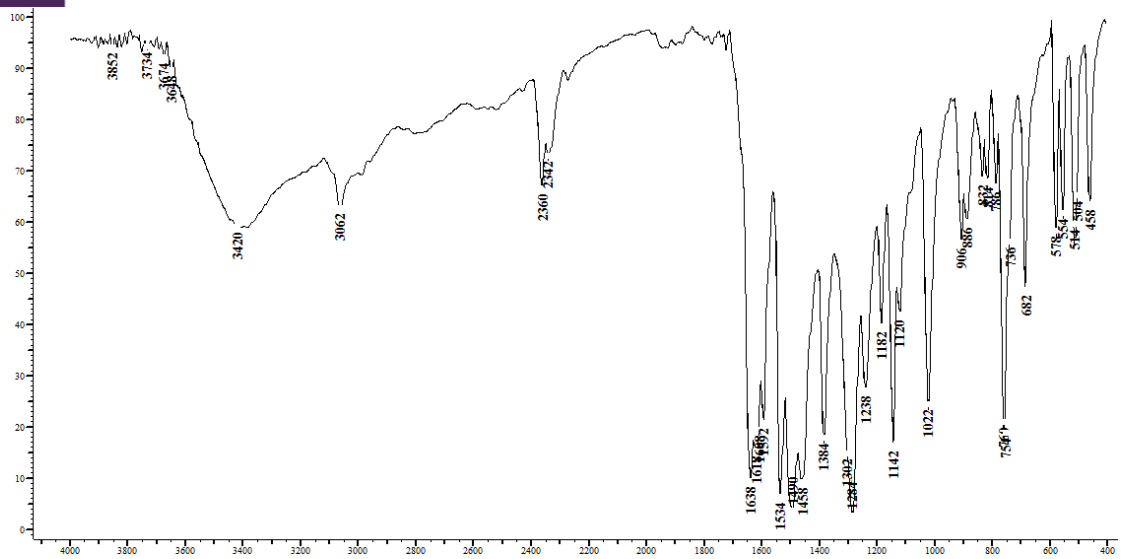

Figure S3. The IR spectrum (KBr, cm^{-1}) of a well dried sample of complex $[Tb(NO_3)_3(salanH)_2(MeOH)]\cdot(salanH)$ (**17**_Tb).

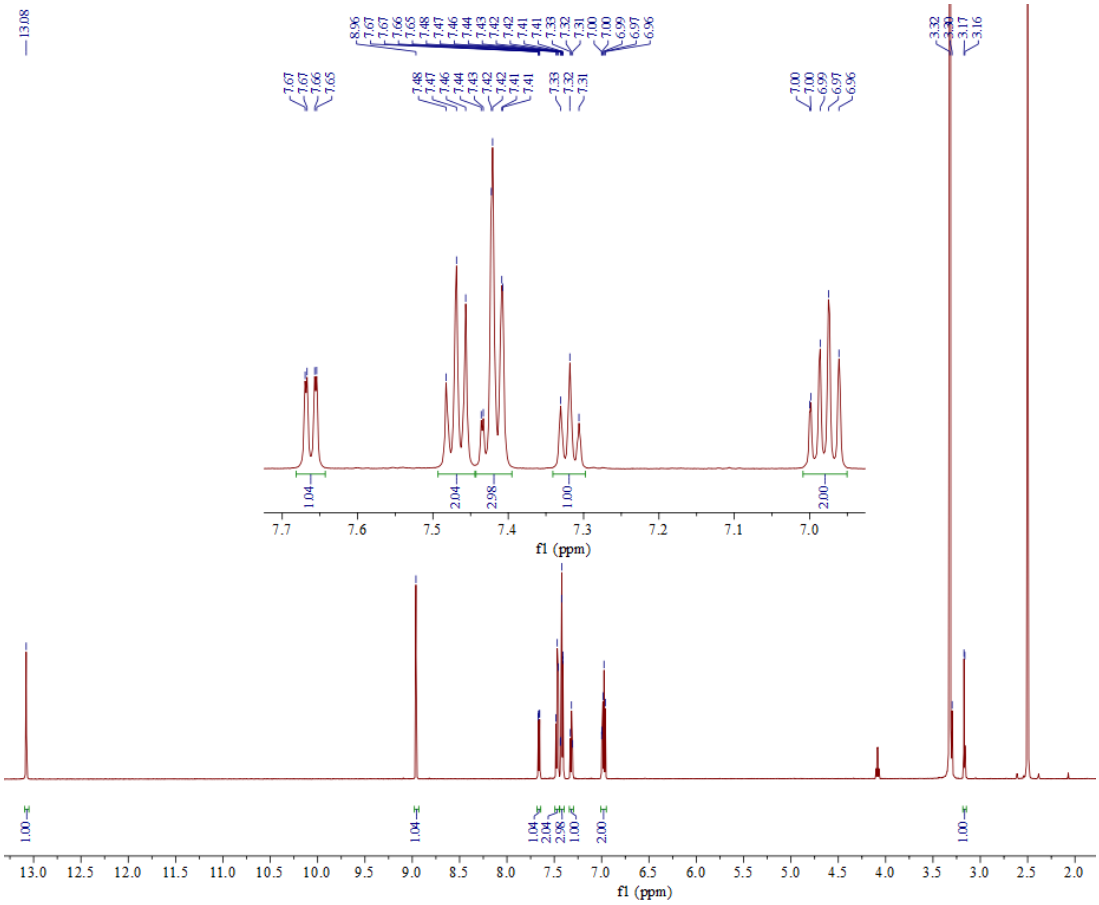

Figure S4. The ^1H NMR spectrum (δ/ppm) of the Y(III) complex **22**_Y in DMSO-d_6; the inset shows the aromatic region in more detail.

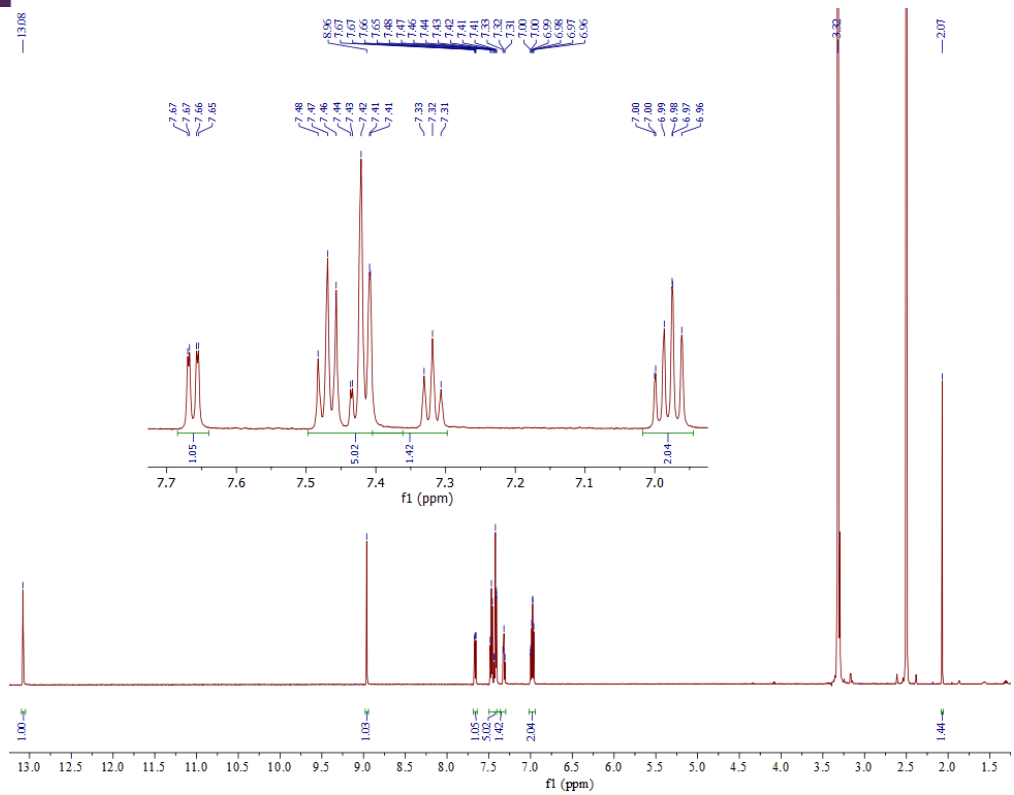

Figure S5. The ^{1}H NMR spectrum (δ/ppm) of a dried sample of complex $[Y(NO_3)_3(salanH)_2(H_2O)]\cdot MeCN$ (**11**·MeCN_Y) in DMSO-d_6; the inset shows the aromatic region in more detail.

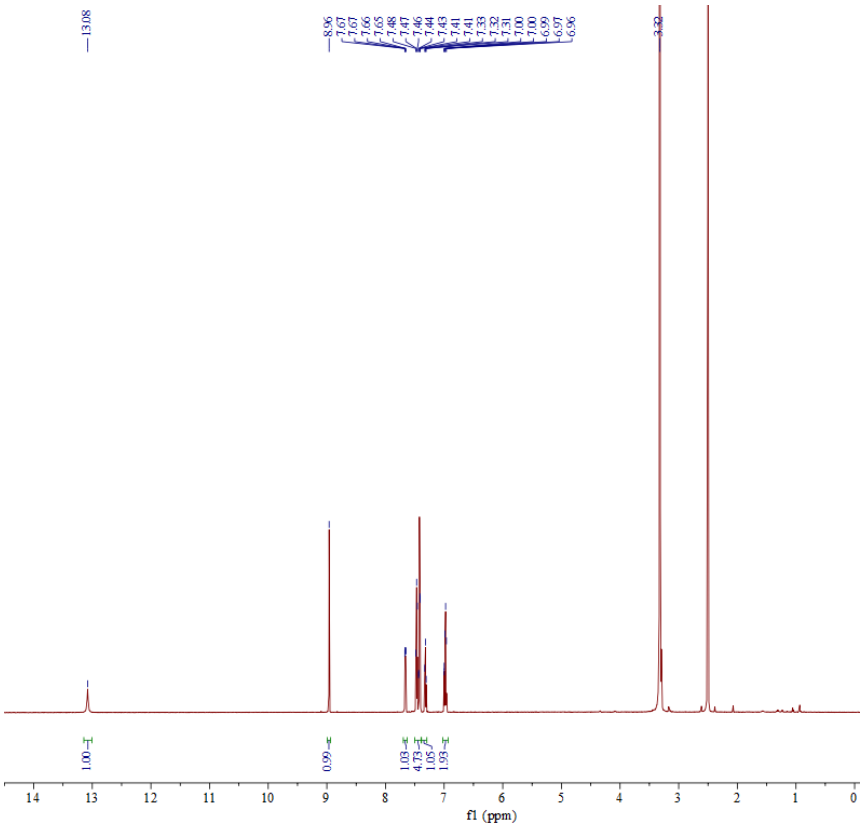

Figure S6. The ^{1}H NMR spectrum (δ/ppm) of salanH in DMSO-d_6.

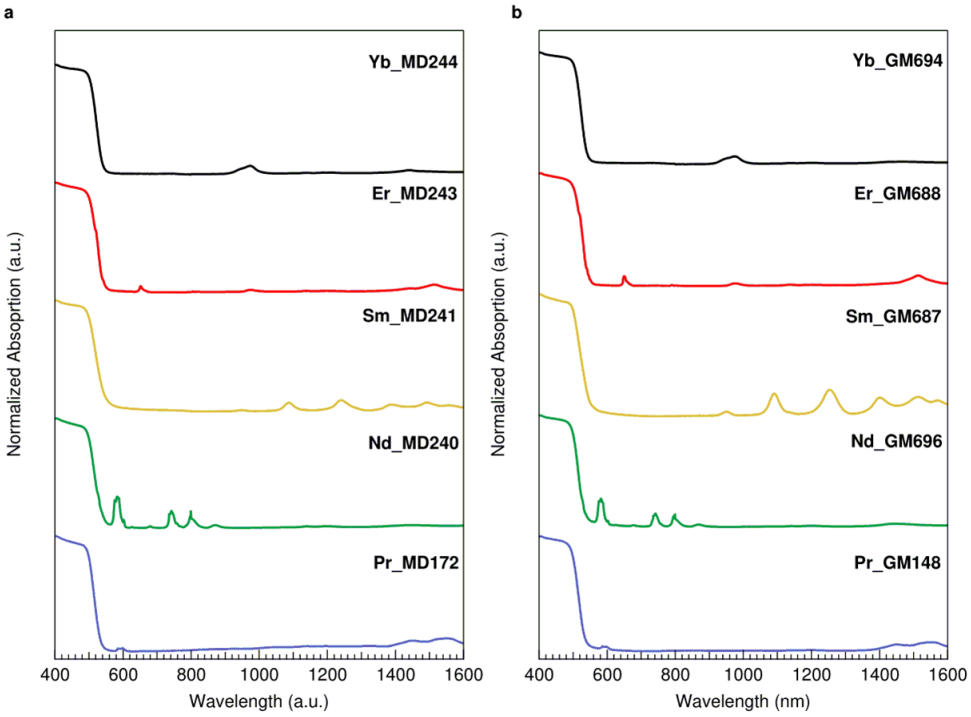

Figure S7. Solid-state (diffuse reflectance) electronic spectra of Ln(III)/salanH complexes isolated from MeOH (**a**) and MeCN (**b**). The codes Pr_GM148, Nd_GM696, Sm_GM687, Er_GM688 and Yb_GM694 correspond to complexes **1**·MeCN_Pr, **2**·MeCN_Nd, **3**·MeCN_Sm, **9**·MeCN_Erand **10**·MeCN_Yb, respectively. The codes Pr_MD172, Nd_MD240, Sm_MD241, Er_MD243 and Yb_MD244 correspond to complexes **12**_Pr, **13**_Nd, **14**_Sm, **20**_Er and **21**_Yb, respectively.

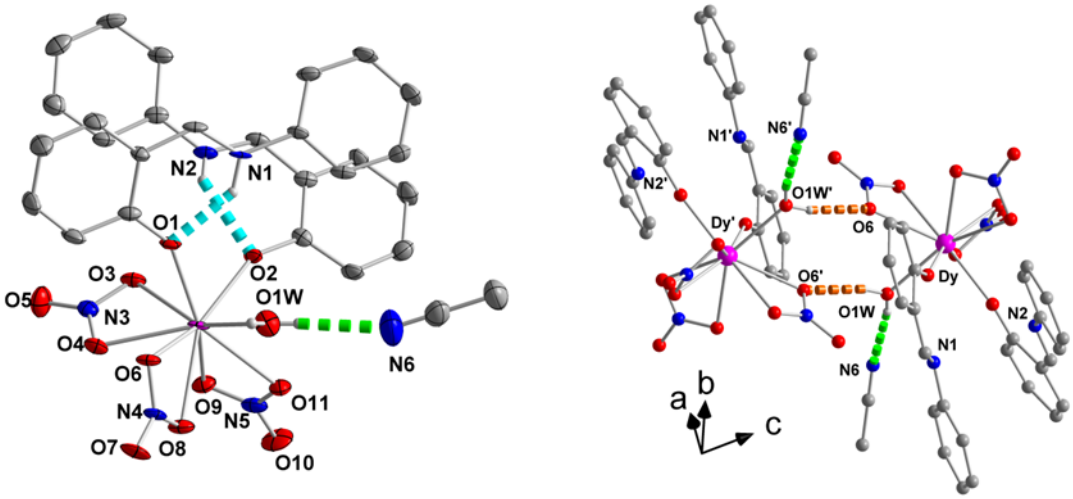

Figure S8. (Left) Partially labelled ORTEP plots of the molecules [Dy(NO_3)$_3$(salanH)$_2$(H_2O)] and MeCN at the 50% thermal ellipsoids probability level that are present in the crystal structure of complex **7**·MeCN_Dy. (Right) A H-bonded {[Dy(NO_3)$_3$(salanH)$_2$(H_2O)]·MeCN}$_2$ dimer in the crystal structure of the same complex. The dashed, cyan lines indicate the intramolecular N1-H(N1)···O1 and N2-H(N2)···O2 H bonds. The dashed, light green and orange lines represent the O1W-H_B(O1W)···N6 and O1W-H_A(O1W)···O6′ (−x + 2, −y, −z + 1) intermolecular H bonds, respectively.

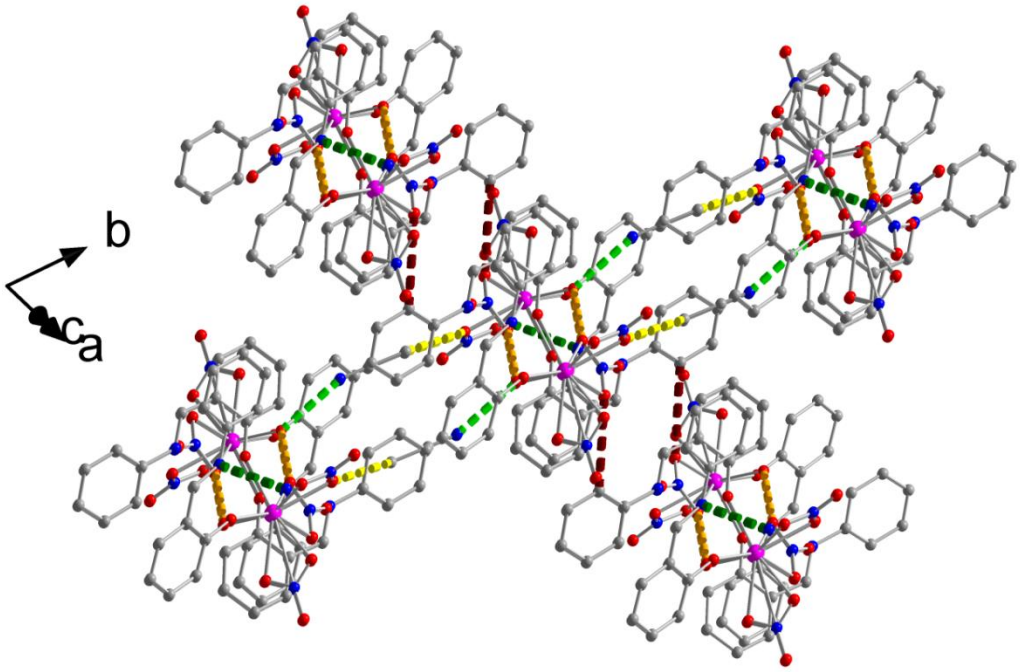

Figure S9. A part of the 3D architecture of complex **7**·MeCN_Dy as seen down the [10–1] crystallographic direction. The dashed, dark red and yellow lines represent the C13-H(C13)···O8''' (x − 1, y, z) and C28-H$_B$(C28)···O4'' (x, y − 1, z) H bonds, respectively. For the color codes of the other intermolecular interactions, see the captions of Figures 8 and S7. Atom C13 is an aromatic carbon atom of the benzylidene (phenolate) ring of one salanH ligand and atom C28 is the methyl carbon atom of the lattice MeCN molecule.

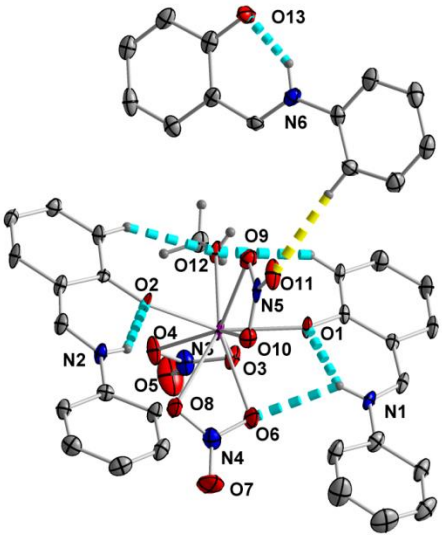

Figure S10. Partially labelled ORTEP plots of the [Dy(NO$_3$)$_3$(salanH)$_2$(MeOH)] and lattice salanH molecules at the 50% thermal ellipsoids probability level in the crystal structure of **18**_Dy. The dashed cyan lines represent the intermolecular N1-H(N1)···O1, N1-H(N1)···O6, N2-H(N2)···O2, C2-H(C2)···O12, C15-H(C15)···O12 and N6-H(N6)···O13 H bonds. The dashed yellow line indicates the C36-H(C36)···O11 intermolecular H bond. Atoms C2 and C15 (not labelled) are aromatic carbon atoms that belong to the benzylidene(phenolate) rings of the two coordinated salanH ligands. Atom C36 is an aromatic carbon atom that belongs to the aniline ring of the lattice salanH molecule. The central Dy^{III} ion has not been labelled.

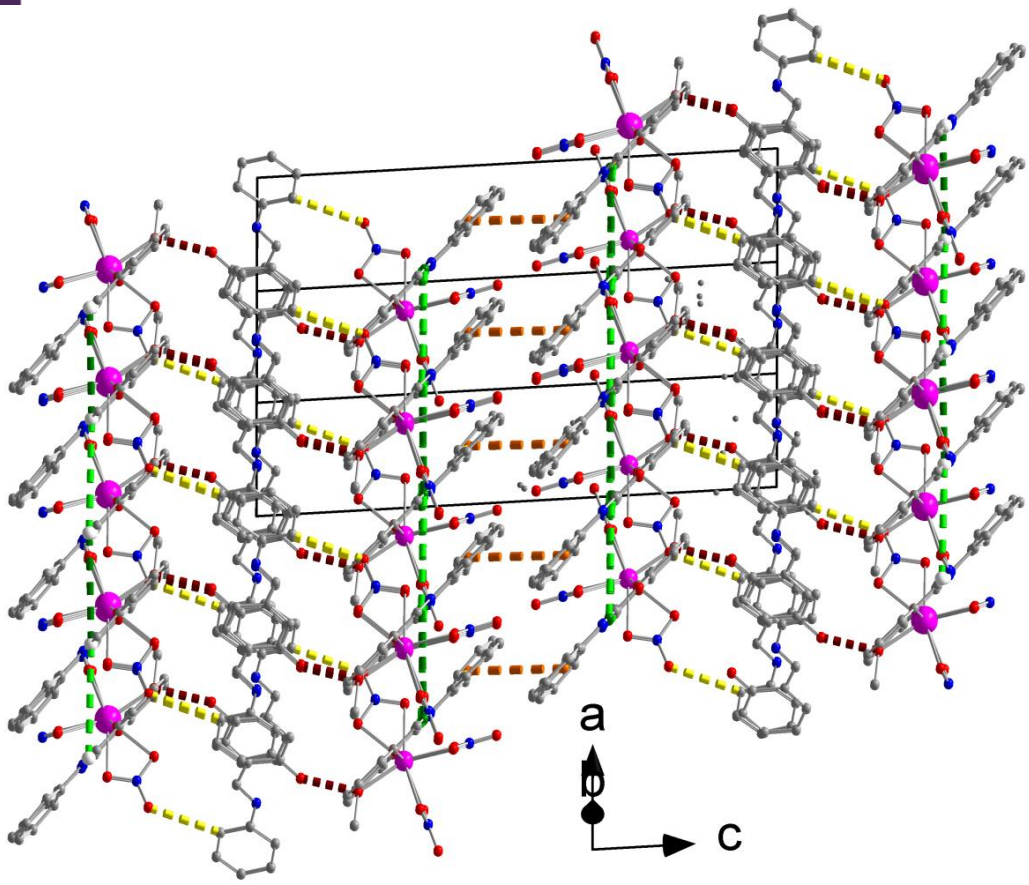

Figure S11. Stacking of layers along the *c* axis in the crystal structure of **18**_Dy. The color code is the same with that used in Figures 8 and 11.

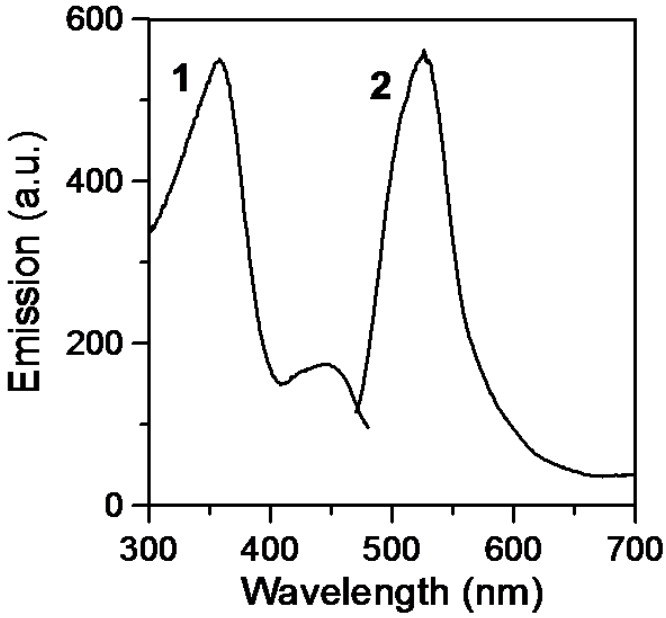

Figure S12. Solid-state, room-temperature excitation (curve 1: maximum emission at 540 nm) and emission (curve 2: maximum excitation at 360 nm) spectra of complex **5**·MeCN_Gd.

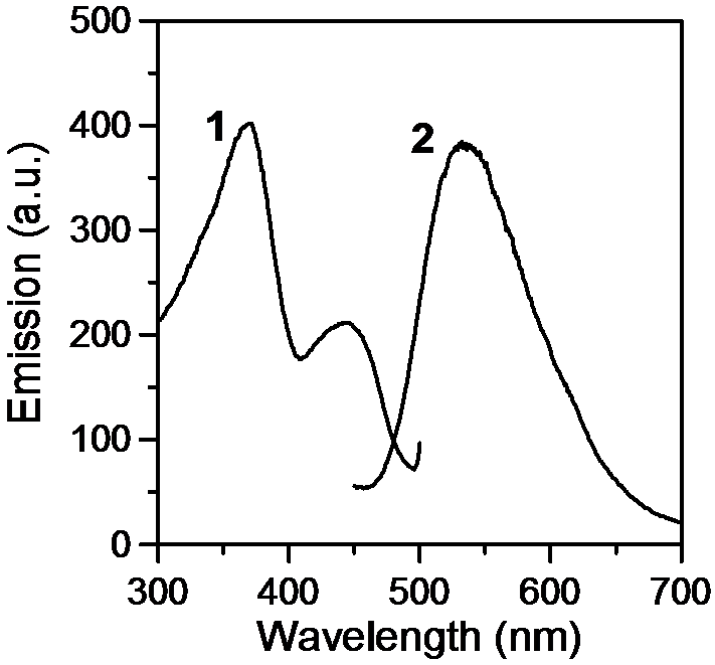

Figure S13. Solid-state, room-temperature excitation (curve 1: maximum emission at 540 nm) and emission (curve 2: maximum excitation at 360 nm) spectra of complex **6**·MeCN_Tb.

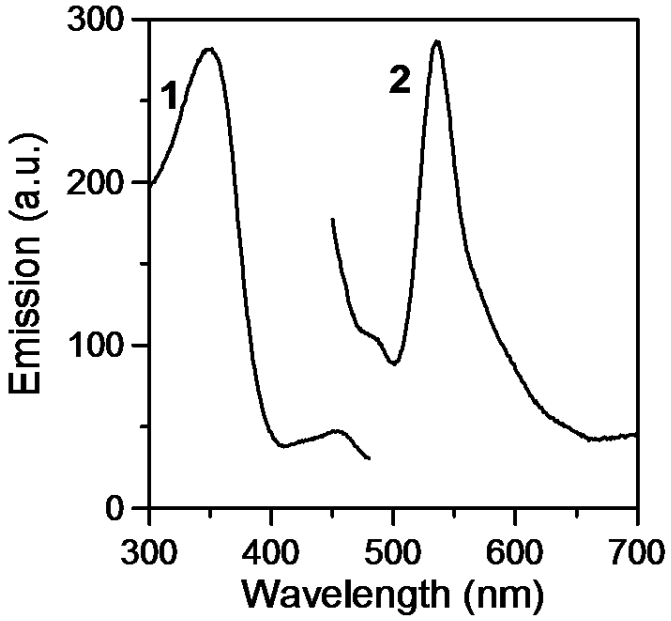

Figure S14. Solid-state, room-temperature excitation (curve 1: maximum emission at 540 nm) and emission (curve 2: maximum excitation at 360 nm) spectra of complex **7**·MeCN_Dy.

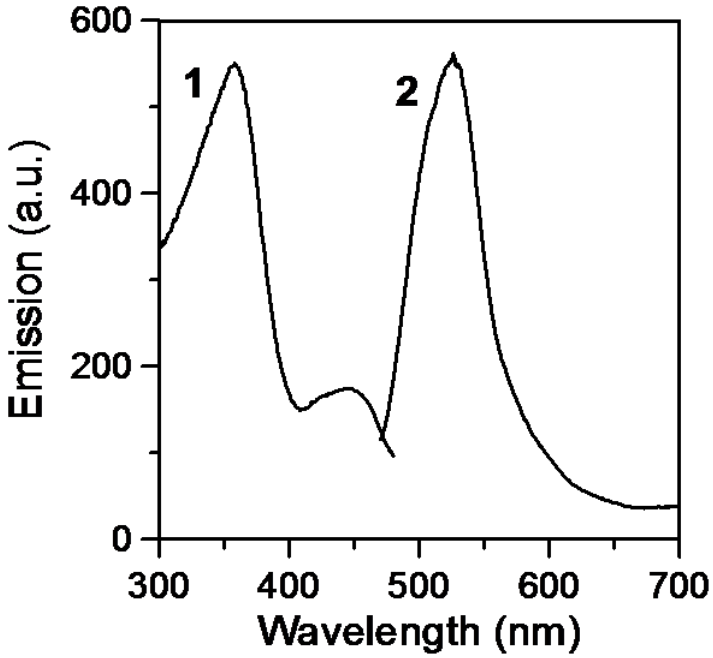

Figure S15. Solid-state, room-temperature excitation (curve 1: maximum emission at 527 nm) and emission (curve 2: maximum excitation at 360 nm) spectra of complex **16**_Gd.

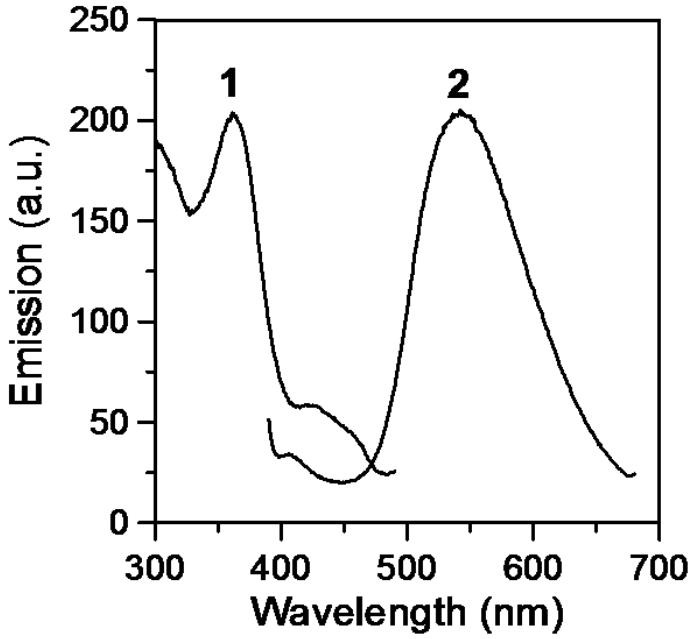

Figure S16. Solid-state, room-temperature excitation (curve 1: maximum emission at 540 nm) and emission (curve 2: maximum excitation at 360 nm) spectra of complex **17**_Tb.

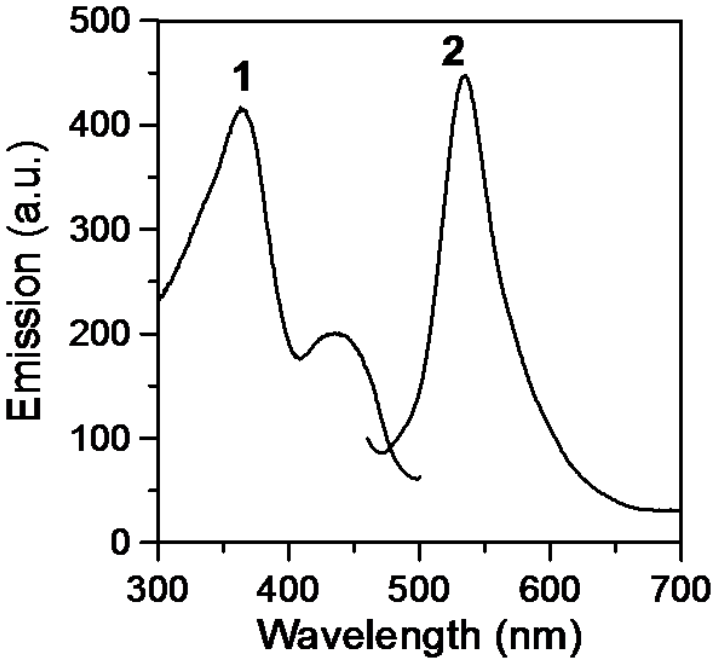

Figure S17. Solid-state, room-temperature excitation (curve 1: maximum emission at 535 nm) and emission (curve 2: maximum excitation at 360 nm) spectra of complex **18**_Dy.

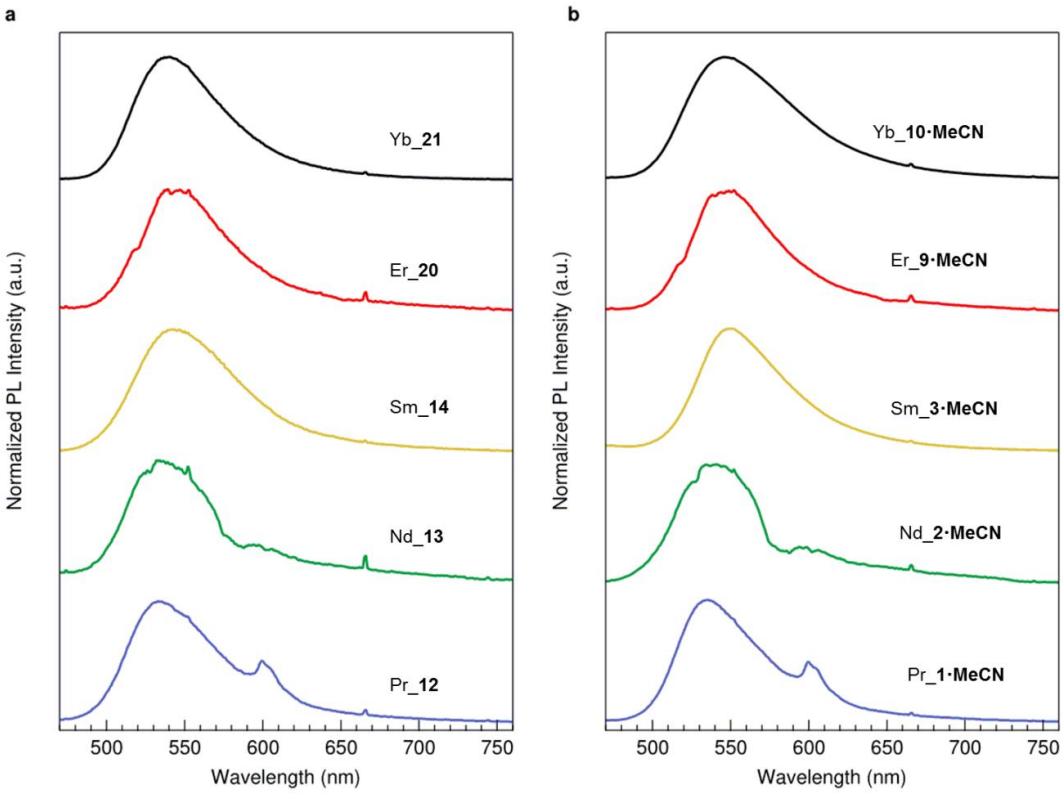

Figure S18. Solid-state, room-temperature visible emission spectra of complexes **1**·MeCN_Pr, 2·MeCN_Nd, **3**·MeCN_Sm, **9**·MeCN_Er, **10**·MeCN_Yb (**b**, right) and **12**_Pr, **13**_Nd, **14**_Sm, **20**_Er, **21**_Yb (**a**, left) upon CW laser excitation at 405 nm.

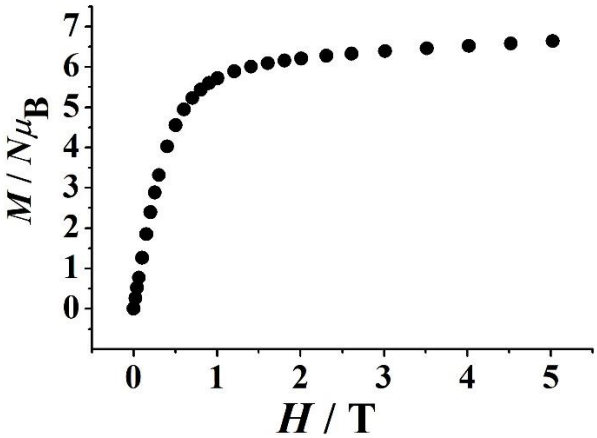

Figure S19. Magnetization vs. field plot for complex **7**_Dy at 2.0 K.

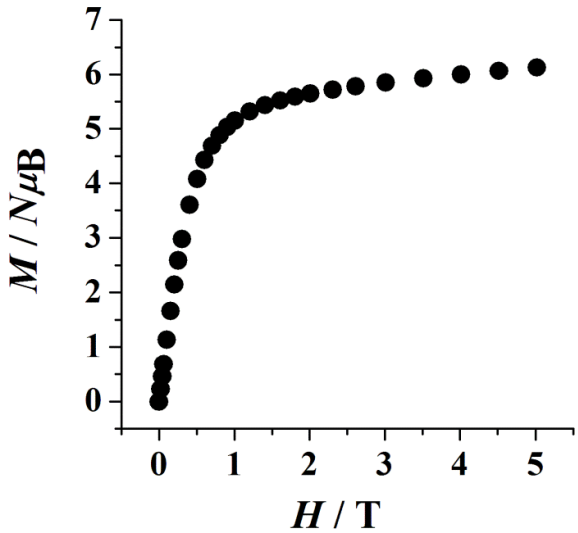

Figure S20. Magnetization vs. field plot for complex **18**_Dy at 2.0 K.

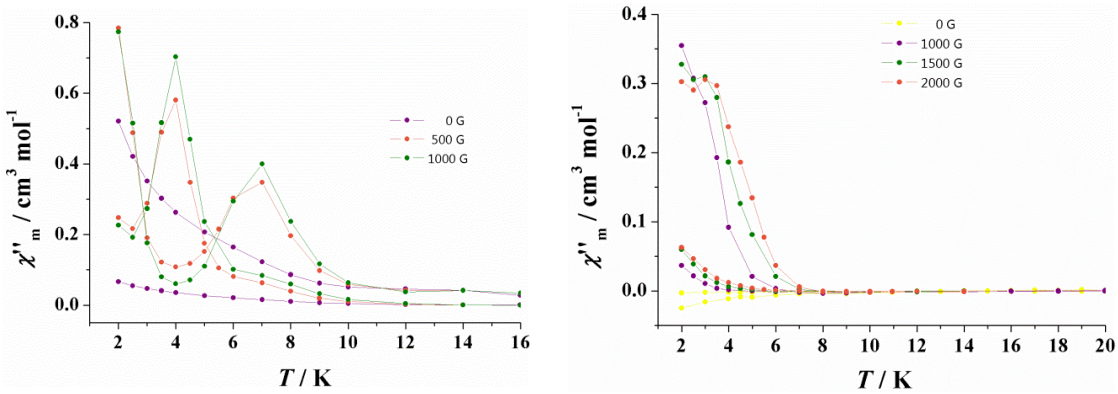

Figure S21. AC measurements for complexes **18**_Dy (left) and **17**_Tb (right) at variable fields. The field that gives the maximum dependence of the ac signal was selected in all cases to perform the complete measurements.

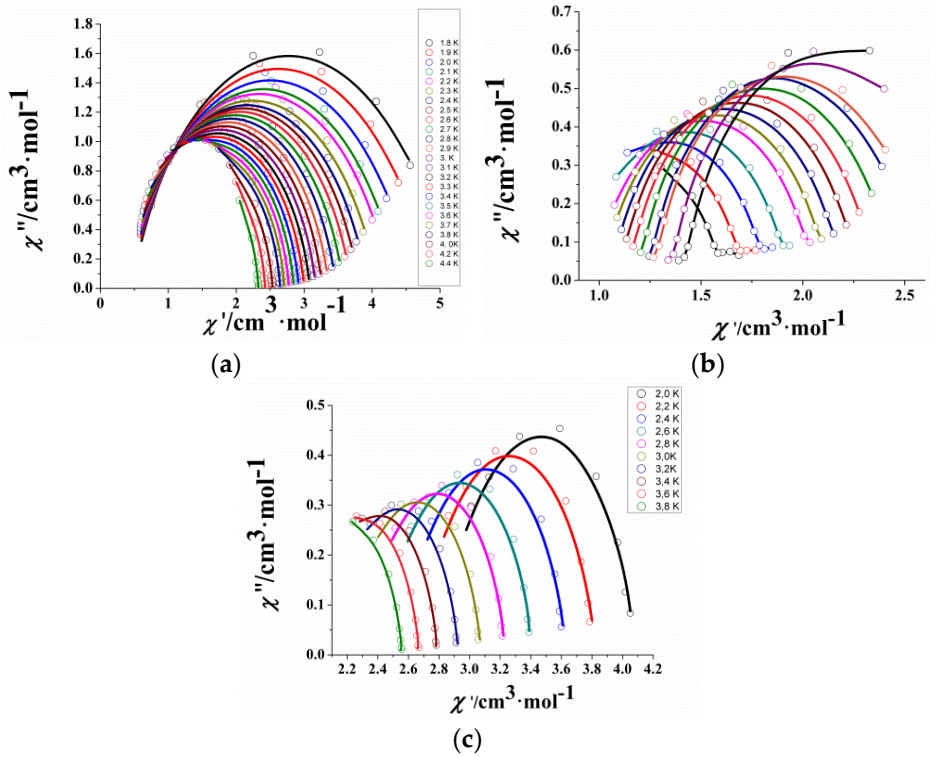

Figure S22. Cole-Cole (Argand) plots for complexes (**a**) **7**_Dy (upper left), (**b**) **18**_Dy (upper right) and (**c**) **17**_Tb (bottom ~~left~~). The solid lines represent the best fit for **7**_Dy and **18**_Tb. The solid lines are guides for the eye in the case of **18**_Dy; a fit with reliable α values was not possible for the latter complex due to the simultaneous existence of two magnetization relaxation pathways.

References

1. Van Wyk, J.L.; Mapolie, S.F.; Lennartson, A.; Håkansson, M.; Jagner, S. The catalytic oxidation of phenol in aqueous media using cobalt(II) complexes derived from N-(aryl) salicylaldimines. *Inorg. Chim. Acta* **2008**, *361*, 2094–2100.
2. Zhou, M.-D.; Zhao, J.; Li, J.; Yue, S.; Bao, C.-N.; Mink, J.; Zang, S.-L.; Kühn, F.E. MTO Schiff-Base Complexes: Synthesis, Structures and Catalytic Applications in Olefin Epoxidation. *Chem. Eur. J.* **2007**, *13*, 158–166.
3. Destro, R.; Gavezzotti, A.; Simonetta, M. Salicylideneaniline. *Acta Crystallogr.* **1978**, *B34*, 2867–2869.
4. Arod, F.; Gardon, M.; Pattison, P.; Chapuis, G. The α_2-polymorph of salicylideneaniline. *Acta Crystallogr.* **2005**, *C61*, o317–o320.
5. Arod, F.; Pattison, P.; Schenk, K.J.; Chapuis, G. Polymorphism in N-Salicylideneaniline Reconsidered. *Cryst. Growth Des.* **2007**, *7*, 1679–1685.
6. Kaur, G.; Singh, S.; Sreekumar, A.; Choudhury, A.R. The evaluation of the role of C-H⋯F hydrogen bonds in crystal altering the packing modes in the presence of strong hydrogen bond. *J. Mol. Struct.* **2016**, *1106*, 154–169.
7. Maniaki, D.; Mylonas-Margaritis, I.; Mayans, J.; Savvidou, A.; Raptopoulou, C.P.; Bekiari, V.; Psycharis, V.; Escuer, A.; Perlepes, S.P. Slow magnetic relaxation and luminescence properties in lanthanide(III)/anil complexes. *Dalton Trans.* **2018**, *47*, 11859–11872.
8. Nakamoto, K. *Infrared and Raman Spectra of Inorganic and Coordination Compounds*, 4th ed.; Wiley: New York, NY, USA, 1986; pp. 254–257.
9. Jain, A.K.; Gupta, A.; Bohra, R.; Lorenz, I.-P.; Mayer, P. Synthesis and structural elucidation of some novel aluminium(III) complexes with Schiff bases: Crystal and molecular structure of $[Al\{O(C_6H_4)CH{=}NC_6H_5\}_2\{HO(C_6H_4)CH = NC_6H_5\}_2]Br$. *Polyhedron* **2006**, *25*, 654–662.
10. Ahmed, Z.; Iftikhar, K. Sensitization of Visible and NIR Emitting Lanthanide(III) Ions in Noncentrosymmetric Complexes of Hexafluoroacetylacetone and Unsubstituted MonodentatePyrazole. *J. Phys. Chem. A* **2013**, *117*, 11183–11201.

11. Carnall, W.T.; Fields, P.R.; Rajnak, K. Electronic Energy Levels in the Trivalent Lanthanide Aquo Ions. I. Pr^{3+}, Nd^{3+}, Pm^{3+}, Sm^{3+}, Dy^{3+}, Ho^{3+}, and Tm^{3+}. *J. Chem. Phys.* **1968**, *49*, 4424–4442.